



## Evaluation of selective laser sintering processes by optical coherence tomography



Guangying Guan<sup>a</sup>, Matthias Hirsch<sup>a</sup>, Zeng Hai Lu<sup>b</sup>, David T.D. Childs<sup>b</sup>, Stephen J. Matcher<sup>c</sup>, Ruth Goodridge<sup>a</sup>, Kristian M. Groom<sup>b</sup>, Adam T. Clare<sup>a,\*</sup>

<sup>a</sup> Manufacturing Division, Faculty of Engineering, University of Nottingham, University Park, Nottingham NG7 2RD, United Kingdom

<sup>b</sup> Department of Electronic and Electrical Engineering, University of Sheffield, Nanoscience & Technology Building, North Campus, Broad Lane, Sheffield S3 7HQ, United Kingdom

<sup>c</sup> Department of Materials Science & Engineering, The Kroto Building, North Campus, Broad Lane, Sheffield S3 7HQ, United Kingdom

### ARTICLE INFO

#### Article history:

Received 21 April 2015

Received in revised form 10 September 2015

Accepted 15 September 2015

Available online 18 September 2015

#### Keywords:

OCT

Selective laser sintering

AM

In-situ monitoring

### ABSTRACT

Selective laser sintering (SLS) enables the fast, flexible and cost-efficient production of parts directly from 3D CAD data. Unlike more established machine tools, there is a marked lack of process monitoring and feedback control of key process variables. In-situ analysis techniques permit the emergence of repair techniques, in-process optimization of production parameters, and will also serve to save time and material. In this study, optical coherence tomography (OCT) is used for the first time to evaluate components produced by SLS. Using a Polyamide-PA2200, surface defects are analyzed and the limiting factors associated with the measurement technique are quantified. OCT is shown to be a useful technique for evaluating surface irregularities alongside sub-surface defects that have resulted from poor sintering or non-homogeneous powder spreading. We demonstrate detection and quantification of surface defects such as cracks, pores and voids on a  $\sim 30 \mu\text{m}$  scale. Furthermore, we show that this technique can resolve 'built-in' fine features within a 200 to 400  $\mu\text{m}$  depth below the surface, covering typical layer thicknesses used by this process. This capability paves the way for real-time monitoring of the SLS process for assurance, or even dynamic correction of defects during the build.

© 2015 The Authors. Published by Elsevier Ltd. This is an open access article under the CC BY license (<http://creativecommons.org/licenses/by/4.0/>).

### 1. Introduction

Additive manufacturing (AM) is an emerging technique that provides an alternative solution to traditional, subtractive manufacturing in many situations where fast and cost-efficient fabrications are required [1]. AM is currently undergoing a transition from application in prototype [2–4] and pilot production technology towards scalable and high-value manufacture of bespoke components. Accelerated uptake will be aided by improved process control and dynamic correction. Selective laser sintering (SLS) is a maturing additive manufacturing technique, first demonstrated in the 1980s [5,6], which enables fast, flexible and cost-effective fabrication of highly complex monolithic polymer parts. The freedom of design afforded by SLS allows significant mass and cost reductions. The rapid set-up and build time enable one of the quickest routes from product design to market launch, which is of benefit to application in the medical sector [7–10], as well as aviation and space industries [11]. However, the SLS process can be affected by a number of factors associated with the properties of the material used and with the sintering process itself [12,13]. For example, temperature, gravity and capillary effects make it difficult to achieve 100%

density in the manufactured elements. Common failure modes in SLS-built parts include: pores and cracks inside or at the edge of specimens, irregular surface finishing, closed holes or gap fusion, missing or thin walls and loose powders inclusion [13]. Such failures, caused by poor sintering or non-homogeneous spreading in previous layers, will result in a reduction of the part's lifetime.

Manufacturing methods for the high value markets (e.g. aerospace, healthcare) are characterised by the level of process monitoring that govern their operation. These are commonly used to 'feedback' into the process to rectify wayward conditions and also 'feed-forward' to help with the specification of rework. Manufacturing of the future is set to be more data rich than it is today with advent of initiative such as "Industry 4.0" and "cloud manufacturing". While process control is common in modern machining centres and available often as a low cost add-on, this technology is yet to be developed for AM tools in any meaningful way. The most significant barrier to the uptake of AM processes is the high cost per part and a lack of confidence in part integrity. Furthermore, where certification of a process is required, assurances must be provided that the product matches specification. Non-destructive evaluation (NDE) methods including X-Ray Computed Tomography (XCT) [14,15] have proven useful for determining the integrity of additively manufactured parts, but are expensive and typically only allow 10–100  $\mu\text{m}$  spatial resolution. In addition, faults originating

\* Corresponding author.

E-mail address: [adam.clare@nottingham.ac.uk](mailto:adam.clare@nottingham.ac.uk) (A.T. Clare).

in the early stages of a lengthy manufacturing run are not recognised until after processing is complete. It is proposed that in-situ analysis techniques will be incorporated into additive manufacturing systems in order to monitor the manufacturing process and identify defects as they occur. This will permit the emergence of repair techniques, closed-loop in-process optimization of production parameters and will also serve to save time and material if a build must be aborted.

Optical coherence tomography (OCT) is a non-contact imaging technique which allows video-rate 3 dimensional (3D) representation of the structure with axial resolutions  $< 10 \mu\text{m}$ . Now widely employed in ophthalmology [16,17], oncology [18,19] and cardiology [20,21], the main drive is towards cost reduction and system performance enhancement to accelerate wider uptake in clinical diagnosis. Fewer reports exist on the use of OCT outside the biophotonics community, but these include the examination of glass-fibre reinforced polymer matrix composites [22], defects in polymer solar cells during roll-to-roll manufacture [23] and the study of fine art [24]. The scope of OCT could be extended to the functional imaging of a large number of materials that are transparent to the wavelength of the light source used, such as polymeric parts, which are broadly transparent in the near-IR. Compared with XCT for the assessment of SLS specimens, OCT has three main advantages. First, OCT can provide 3D volume images with spatial resolution  $< 10 \mu\text{m}$  compared with  $\sim 50 \mu\text{m}$  for typical XCT. It therefore has the potential capability of imaging single powder particles, as well as measuring pores or voids typically found inside SLS parts. Second, with development of computer processing and optical sensor technology, the scanning speed of OCT could reach speeds of 100 kHz, which will allow more than 390 frames/s. That is, real-time monitoring of the SLS procedure could be achieved due to the high scanning speed. Third, an OCT system could be easily integrated within an SLS system in order to enable in-situ analysis. Since the only elements of the OCT system that need to be inside the working space consists of a galvo mirror, an optical fiber and a small optical train. Compared to XCT systems, current class are of the order of  $2200 \text{ cm}^3$  in their most compact form. It is therefore difficult to envisage an entire XCT technology being integrated within the SLS system in this way.

In this study, OCT is used for the first time to assess components produced by SLS with commercially available polyamide 12 laser sintering material (PA2200, EOS Ltd). Specimens with different features and failure modes were fabricated and measured using the OCT system in order to test the feasibility of using OCT to examine polymeric parts. OCT is therefore demonstrated as a process control tool for SLS.

## 2. Methods and materials

### 2.1. OCT system

In this work we utilize a commercially available, multi-beam, Fourier-domain, swept source OCT system (EX1301, Michelson Diagnostics, Kent, UK). The simplified schematic diagram of this system is shown on Fig. 1. The OCT system is equipped with a laser with a central wavelength of  $1305 \pm 15 \text{ nm}$  and a sweep range of 150 nm at 10 kHz (HSL-2000, Santec, Japan). The axial optical resolution when applied to polyamide PA2200 is  $< 10 \mu\text{m}$ , while the lateral optical resolution, determined by the system optics, is approximately  $7.5 \mu\text{m}$ . The maximum scan width is 7 mm with a penetration depth of up to 2 mm when applied to biological tissues. Common commercially available OCT light sources have central wavelength at 800 nm, 1000 nm and 1300 nm respectively. The penetration depth decreases with wavelength and is work piece material dependant. Therefore, the 1300 nm light source was chosen as it could provide the maximum penetration (measured  $\sim 400 \mu\text{m}$ ) of polymeric material (i.e. multiple layers of sintered powder), whilst offering a resolution capable of resolving individual powder particles, typically  $> 30 \mu\text{m}$  in size.

OCT performs cross-sectional imaging by measuring the magnitude and echo time delay of backscattered light. Cross-sectional images are generated by performing multiple axial measurements of echo time delay (axial scans or A-scans) and scanning the incident optical beam transversely. This produces a two-dimensional data set, which represents the optical backscattering in a cross-sectional plane through the tissue. Images, or B-scans, can be displayed in false color or grey scale to visualize tissue pathology. Two scanning modes may be used for imaging. In the free-run mode, the laser beam is scanned only in one

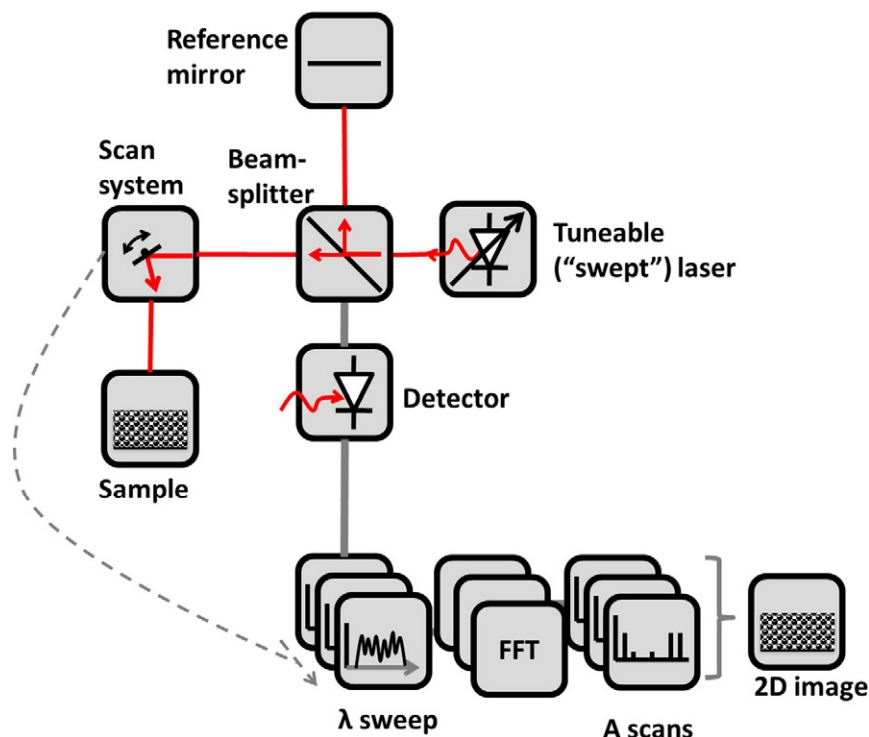


Fig. 1. Schematic diagram of a typical swept laser OCT setup.

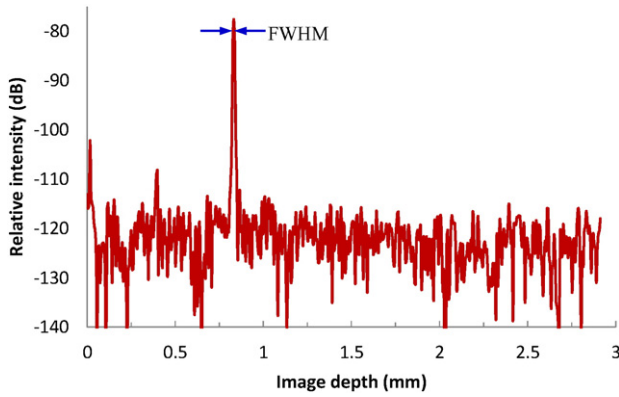


Fig. 2. Typical spectrum of an optical mirror captured by OCT.

direction, acquiring B-scans (frame images) which consist of 1667 A-scans. The OCT beam is overlaid with a red tracer beam, allowing the precise location of the scan to be visualized by the operator. This free-run mode is often used to locate regions of interest that can then be scanned in the other scanning mode: multi-scan. The multi-scan mode captures sequences of images (i.e. B-scans) at set positions decided by a motorised stage holding the sample. The operator can set the number of slices in the sequence and the slicing spacing, which produces a three-dimensional scanned volumetric data set.

## 2.2. Resolution measurement

The axial (depth) resolution of the OCT system is defined as the smallest distance that can be discriminated between two refractive index discontinuities. This resolution is determined by the coherence length of the light source. The coherence length,  $l_c$ , is the spatial width of the field autocorrelation interferogram and can be determined by the Fourier transform of the source power spectrum. The axial resolution,  $\delta z$ , is inversely proportional to the optical bandwidth, and is determined by the following relationship:

$$\delta z = l_c = \frac{2 \ln 2 \lambda_0^2}{\pi \Delta \lambda} \quad (2.1)$$

where  $\Delta \lambda$  is the optical bandwidth, of the light source (assuming a Gaussian spectrum) and  $\lambda_0$  is the centre wavelength. The actual axial and lateral resolutions of the EX1301 OCT system were measured before specimen characterization. A planar optical mirror was used as the target for the axial resolution measurement. Fig. 2 shows the captured coherence spectrum when the mirror is placed at the best focus plane, which was set to be 0.8 mm below zero path length difference of the delay line. The axial resolution was defined by the full width half maximum (FWHM) which was  $8.8 \mu\text{m}$  in air at the plane of best focus.

The lateral resolution in OCT, as in microscopy, is determined by the focusing optics of the light incident on the sample. Assuming an ideal Gaussian beam, the lateral resolution,  $\Delta x$ , is the diffraction limited spot size on the sample and is given by:

$$\Delta x = \frac{4\lambda_0 f_{obj}}{\pi d} \quad (2.2)$$

where  $f_{obj}$  is the focal length of the objective lens and  $d$  is the beam waist of the beam on the objective lens.

A positive USAF1951 resolution test pattern was used as a test target to obtain a volumetric 3D image at the best focus plane. Fig. 3 (left) shows the 90.5 line-pairs-per-mm element resolved (element 4, group 6, each bar is  $5.5 \mu\text{m}$  wide). For quantitative analysis, we measured a modulation depth of 15% using element 4 of group 6 in the USAF1951 test target in air (Fig. 3 (right)). For a Gaussian beam, this implies a FWHM spot size of around  $8.4 \mu\text{m}$ .

## 2.3. Sample preparation

The test parts analysed in this investigation were fabricated using commercially available polyamide 12 laser sintering material (PA2200, EOS Ltd) in a FORMIGA P 100 SLS system (from EOS e-Manufacturing Solutions). Four sets of test parts were designed to mimic the different types of failure modes typical in SLS-produced parts. The composition and purpose of each set of test parts are summarised in Table 1. Group 1 consists of solid parts with smooth surfaces and no internal voids or other features designed in; group 2 includes similar parts from group 1 but with a range of different voids opened on the surface; group 3 contains parts with areas containing loose powder on the surface; group 4 contains specimens with similar voids as those in group 2, however in this case the voids are designed to reside approximately  $100 \mu\text{m}$  below the surface.

## 3. Results

### 3.1. Surface roughness characterization using OCT

The specimens in group 1 were designed to have a smooth surface. However, protuberances may occur during the fabrication procedure, such as that observed in Fig. 4(a). The profile of this protuberance can be observed in the cross-sectional image in Fig. 4(b), which shows a slice through the cross-section, A-A, in Fig. 4(a). A topographical plot can be constructed from the OCT data set and is shown in Fig. 4(c), providing a detailed, scaled representation of the protuberance.

### 3.2. Surface void detection using OCT

A specimen from group 2 incorporating different shapes of voids was analyzed by both scanning electron microscopy (SEM) and OCT. This

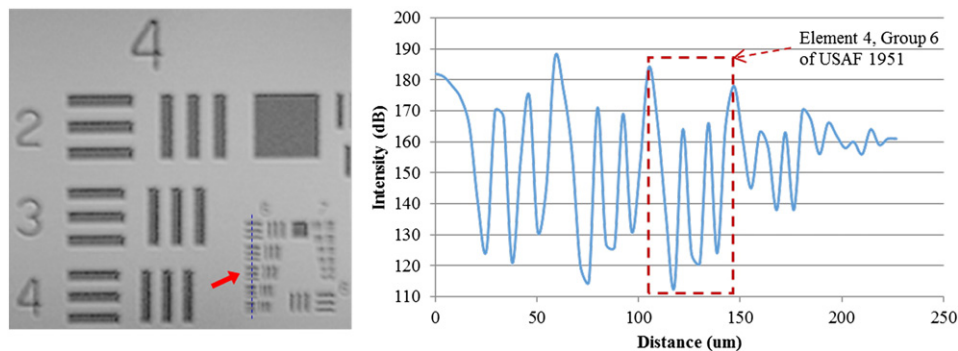


Fig. 3. An OCT volumetric/C scan of a USAF1951 target (left) shows the 90.5 line-pairs-per-mm element resolved (each bar is  $5.5 \mu\text{m}$  wide). An example profile across elements in group 6 as marked in blue dash line is plotted (right) for quantitative analysis.

**Table 1**  
Summary of structure type investigated.

Specimen name	Description	Purpose
Group 1	Solid specimens with smooth surface	Surface analysis
Group 2	Solid specimens with open voids	Surface defects analysis
Group 3	Solid specimens loose powder area	Powder vs. fused material analysis
Group 4	Solid specimens with different shapes of void below surface	Subsurface defect detection

specimen was designed to include a regular, square-shaped void. However, the parts fabricated by the SLS system suffered several unintentional defects. It can be observed from Fig. 5(c) and (d) that a large number of protuberances, similar to those in 3.1 above, exist at the top surface and at the bottom of each void. We attribute these protuberances to poor sintering or non-homogeneous spreading in previous layers. Fig. 5(b) shows the 3D volumetric image of the regular void area, which we display on a zoomed-in scale in Fig. 5(d) in order to better compare with the SEM image in Fig. 5(c), which both indicate a shallower than designed void. From Fig. 5 (e) we also observe a tapering of the lateral size of the ‘square’ void, which becomes wider towards the surface, as well as a void depth measured as  $\sim 360 \mu\text{m}$  instead of the 5 mm depth as per the design intent. This is commensurate with the findings of the SEM examination in figure (c).

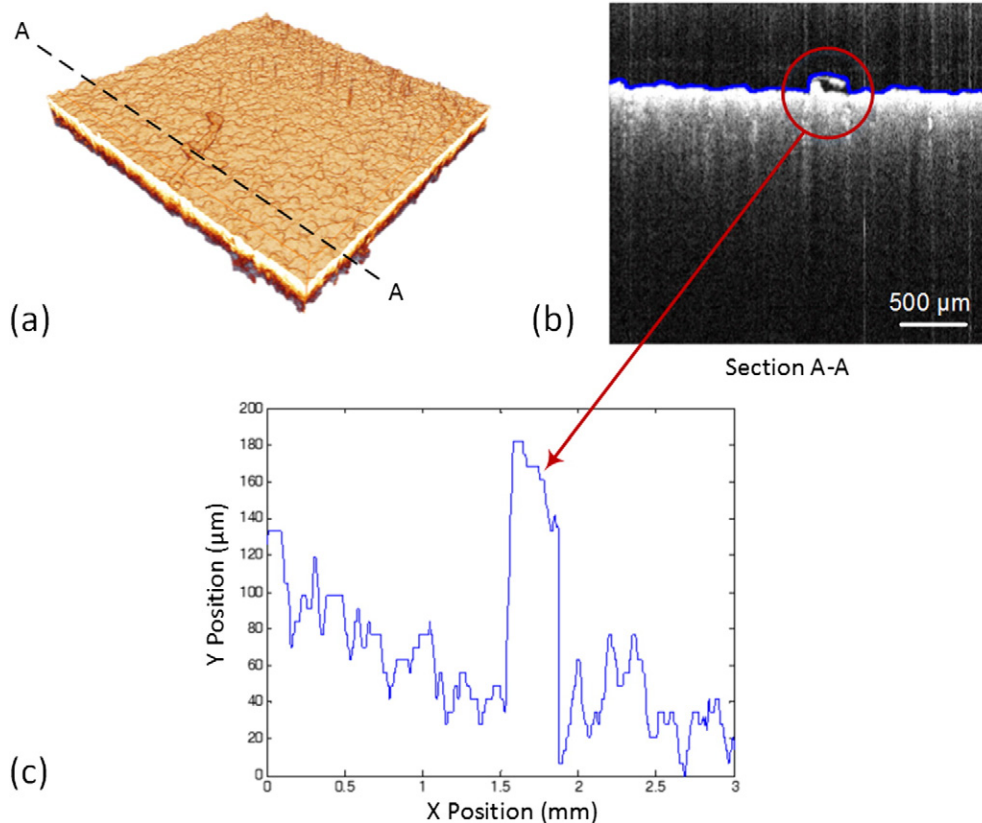
Further experiments were performed to measure the size of individual PA2200 powder particles. The manufacturer's technical specification data gives the average grain size as  $56 \mu\text{m}$ , however a range of particle sizes can be measured from  $28 \mu\text{m}$  to  $92.6 \mu\text{m}$  by SEM, shown in Fig. 6 (top), in which powder was thinly distributed upon a piece of paper (fibrous background). The EX1301 OCT system with a measured lateral resolution of  $8.4 \mu\text{m}$  also demonstrates its capability to detect individual

powder particles as small as  $30 \mu\text{m}$  (Fig. 6 (bottom)). These results may explain why a large number of protuberances can be detected at the surface of specimens such as in Fig. 5 (d), through non-uniformities in local melt dynamics.

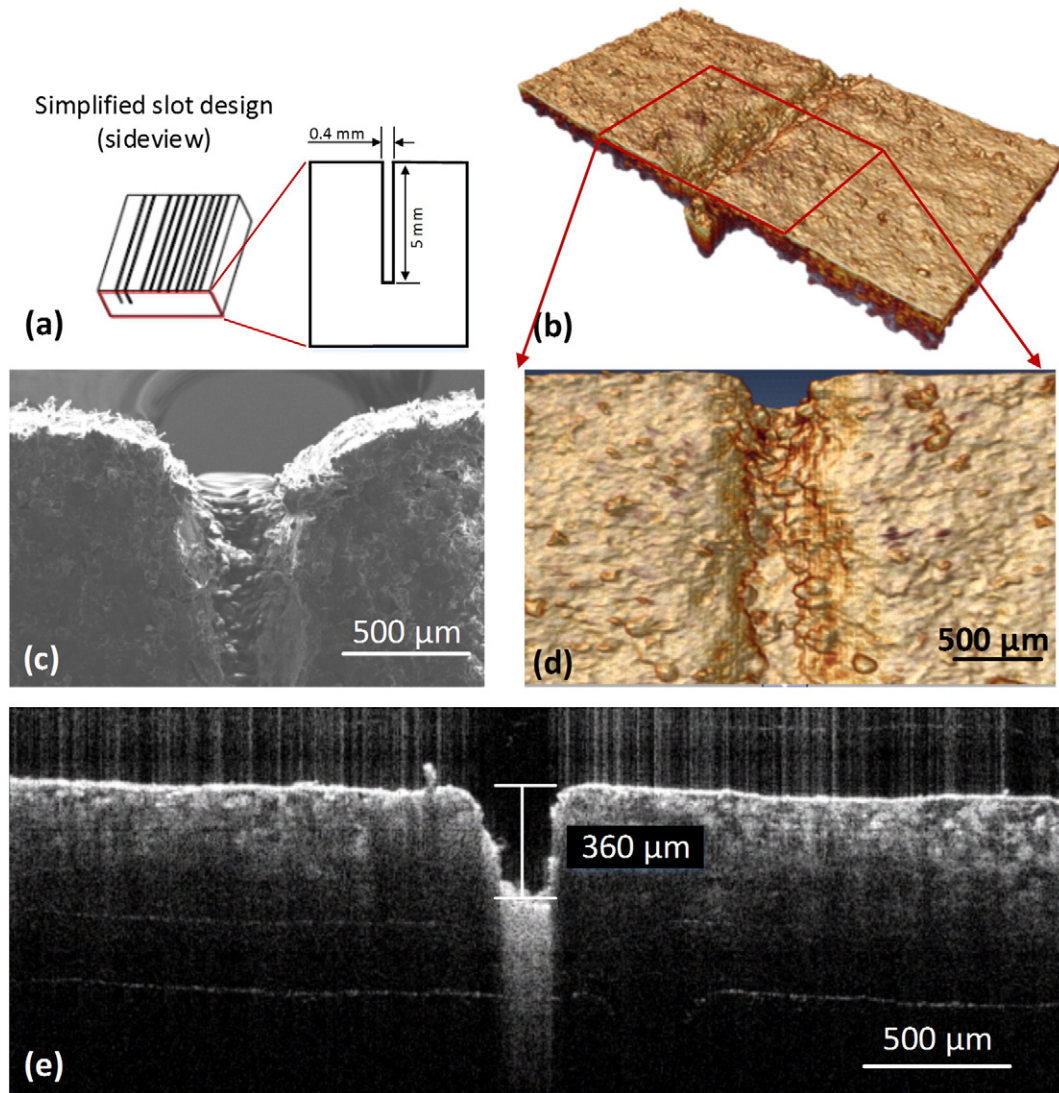
### 3.3. Loose powder detection using OCT

Fig. 7 shows the OCT results and analysis for specimens with both solid (i.e. sintered) and loose (non-sintered) areas. The OCT signal is derived from the back-scattering of light from this sample, hence higher intensity is as a result of higher back scattering properties. Fig. 7 (b) shows an OCT cross-sectional image of the section A-A in (a), through a deep cylindrical void, filled with non-sintered powder. It can be observed from Fig. 7 (b) that the average intensity level within the loose powder area (within the two red dash lines) is much higher than the intensity of the surrounding solid area. The depth-resolved intensity changes from section B-B, C-C and D-D are shown in Fig. 7(c). One OCT B-frame image consists of 1667 A-lines with equal spacing of  $4.2 \mu\text{m}$ . 10 adjacent A-lines from each section are averaged in order to enhance the signal-to-noise ratio. From section B-B and section C-C, it can be observed that the attenuation of intensity within the loose powder area occurs at a much slower rate than the corresponding solid area. An intensity peak, marked by the red dashed circle in Fig. 7(c), which is about  $200 \mu\text{m}$  below the specimen surface can be observed from section D-D. This peak could be caused by encased loose or semi-sintered powder. The expanded scale on section D-D better demonstrates the appearance of the high intensity feature, attributed to a suspected incorporation of a region of loose powder below the specimen's surface.

Quantitative analysis was performed by applying an exponential curve fit to the intensity profile of each section in Fig. 7(c). The highest peak from each section represents the location of the surface. The



**Fig. 4.** Analysis of a solid specimen with smooth surface finishing: (a)  $3 \times 3 \times 3 \text{ mm}$  3D OCT structural image. The corresponding cross-sectional profile through the protuberance A-A in (a) is shown in (b) where the blue line shows the surface of specimen; (c) plots the surface profile shown in (b).



**Fig. 5.** (a) Design of solid specimen with different shapes of void built into the surface of the structures; (b) 3D OCT image of the square void; (c) 2D scanning electron microscope (SEM) image for the square void; (d) zoomed in 2D OCT surface image of the square void; (e) OCT cross-sectional image of the square void.

consecutive 15 pixels below the surface were abandoned for the fitting in order to eliminate the high reflection from the air-sample interface. The cut off intensity threshold was set to 15% of the peak value to avoid the artifact signal originating from deeper within the sample. The  $1/e$  values for curve 1 (loose powder) and curve 2 (solid part) are 0.38 and 0.15 mm respectively. If this drop off were purely due to absorption in polyamide, then the ratio of the two implies a loose power density 39% compared to that of the solid part. This value is as expected since the packing density of mono sized random loose powder cannot exceed 64% [25], and 'rough' polyamide powder without vibration or shaking, is likely to have a much lower density than this upper limit.

By inspection of the cross section D-D in Fig. 7(c), we can see at least two regions of interest. Near the surface, at a position of 0.4 mm, the decay (fitted by curve 3) is in agreement with that of the solid polymer, however, at a position of 0.6 mm an increase in intensity followed by a second decay rate (fitted by curve 4) is seen. This intensity increase corresponds to a large difference in refractive index giving rise to a strong reflection. After this increase, the drop off is significantly lower than that found both near the surface, suggesting an inclusion of loose powder. From curve 4, the attenuation coefficient for the suspected loose powder area is 35% that of the solid part.

### 3.4. Sub-surface feature detection using OCT

Further experiments were performed in order to determine the capability of OCT for the detection of sub-surface features. Two sets of specimens from group 4 were manufactured with a range of different shapes and sizes (in the 100 to 500  $\mu\text{m}$  range) of voids built into the structure at different depths. Fig. 8(b) shows the 3D volumetric structural image measured by XCT with a spatial resolution of 56  $\mu\text{m}$ . A number of voids can be observed at the top area of the cross-section image from (b), however they are blurred due to the small size relative to the large spatial resolution of XCT. One of the largest voids, which is located  $\sim 100$   $\mu\text{m}$  below the surface and has an inverted triangular shape, is marked in Fig. 8(b) by the red circle. The dimensions of this void channel are provided in Fig. 8(a). Fig. 8(b) shows the OCT 3D structural image ( $3 \times 3 \times 0.4$  mm) of the region containing the triangular void, with a section removed from the top quarter of the image to reveal the detailed structure beneath the surface. This triangle is not easily discerned in this figure, however, examination of the constituent *en-face* images reveals the triangular structure more clearly. Fig. 8(d)–(h) show the *en-face* view of this sample at different depths. The brighter regions signify the boundary of the triangle whilst the dark areas signify the void, which is shown to become narrower with

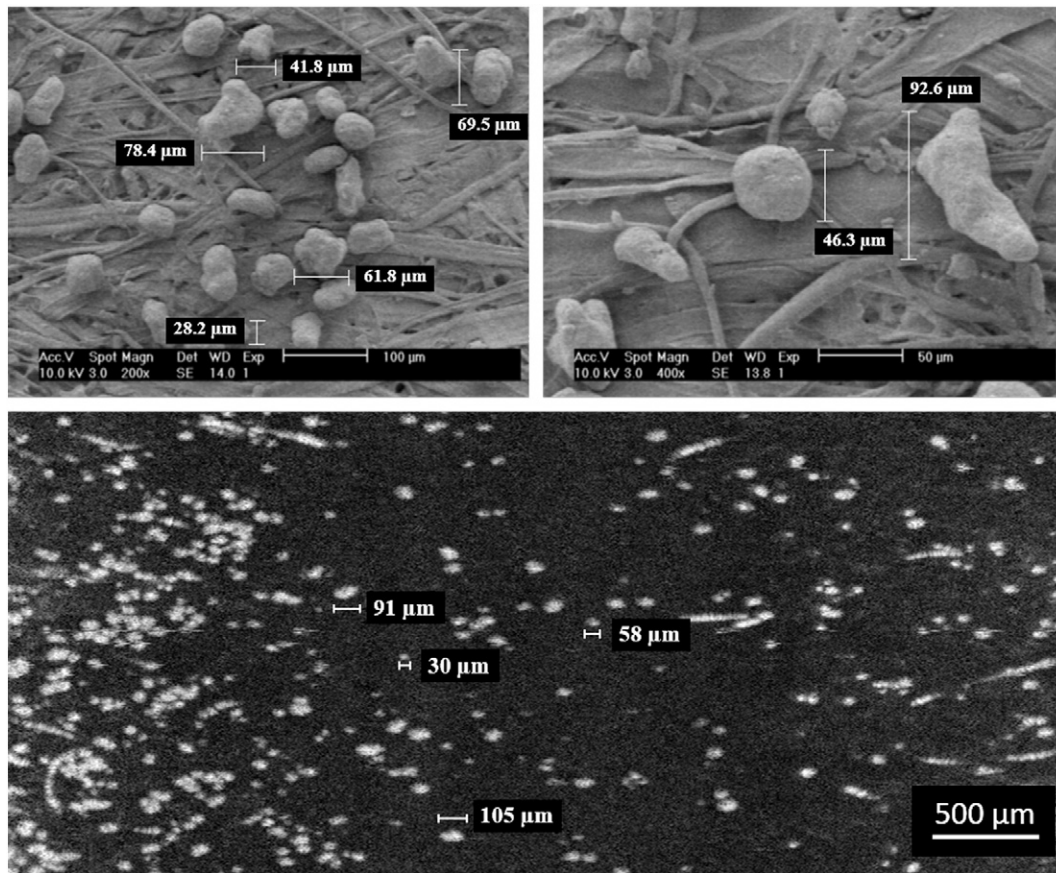


Fig. 6. SEM image of individual PA2200 powder particles (top); OCT en-face image of individual PA2200 powder particles (bottom).

increasing depth below the surface. The void depth measured from Fig. 8(c) is  $\sim 140 \mu\text{m}$ , which is a little shallower than the original design, with this apparent inability to fabricate features with great accuracy/resolution consistent with the surface void example described in 3.2.

Finally, another set of specimens from group 4 were examined. These comprise  $3 \times 3 \times 1 \text{ cm}$  cubes incorporating 12 different shapes of void channels located  $\sim 100 \mu\text{m}$  below the solid surface. The gap between each void channel is 2 mm. In order to further investigate this series of sub-surface features, a scanning protocol was invoked whereby the scanning area was dissected into a series of  $4 \times 3 \text{ mm}$  sections. A schematic diagram illustrating one such 3D section is shown in Fig. 9(a), as described in Section 2.1. A galvo mirror is employed to achieve one B-scan in the  $y$  direction; two translation stages are adapted respectively to realize 3D scanning in the  $x$  direction and bulk moving in the  $y$  direction for the next volume scan. Fig. 9(b) shows the detailed dimensions and locations of three chosen voids. Fig. 9(c) and (d) show the adjacent B-frame OCT cross-sectional images of these chosen voids (marked by red circles) in one 3D scanning section. The triangular and square shaped voids can be easily observed and their depth-resolved dimension can be measured from Fig. 9(c). In addition, the dimensions of voids in the  $x$  direction and the distance to the surface in the  $z$  direction can also be measured easily. The dimensions of the circular channel can be observed and measured in Fig. 9(d). Fig. 9(e) and (f) show the corresponding SEM images of the edge of the triangular and square voids respectively, which provide cross-validation of the OCT measurement. The designed thickness for the top surface layer is  $100 \mu\text{m}$ , however the results from both SEM and OCT demonstrate that the actual thickness is  $\sim 185 \mu\text{m}$ , which can be found in Fig. 9(c-f), and is consistent with the previous measurement of

smaller voids than originally designed. This further highlight the poor manufacturing tolerances associated with SLS when compared to established manufacturing techniques.

#### 4. Discussion

XCT is a commonly used post-process NDE tool, employed to evaluate the quality and integrity of parts produced by SLS. However, the spatial resolution for XCT is presently limited to  $\sim 60 \mu\text{m}$ . SEM can achieve resolutions of  $\sim 10 \text{ nm}$ , making it a powerful tool for defect evaluation of parts after fabrication. However, SEM can only obtain information from the surface of conductive samples, so samples have to be sectioned for internal examination, thereby destroying parts in order to investigate their internal composition. Larger sample sizes would also not fit inside the SEM sample chamber. Furthermore, the equipment size, cost, and scan duration of both these methods would preclude their use in real-time in-situ monitoring.

OCT is an emerging and rapidly developing non-contact optical imaging method which provides real time, depth resolved cross-sectional images with micron scale resolution. Due to its high resolution and non-destructive nature, OCT has been widely used in clinical diagnosis and biological research. To the best of our knowledge, this is the first time that OCT has been applied to probe additively manufactured parts. In Section 3.1 we demonstrated that OCT can capture high-resolution ( $\sim 9 \mu\text{m}$ ) 3D volume images. The EX1301 OCT system we employed for this study can achieve frame rates of 6.25 frames/s with 1600 A-line scans in one B-frame. For real-time monitoring of the SLS printing process for a large sample, this speed will not be sufficient. However, 500 kHz OCT systems [26] are now available, offering 25 times faster scan rate than the EX1301. In addition, we can perform

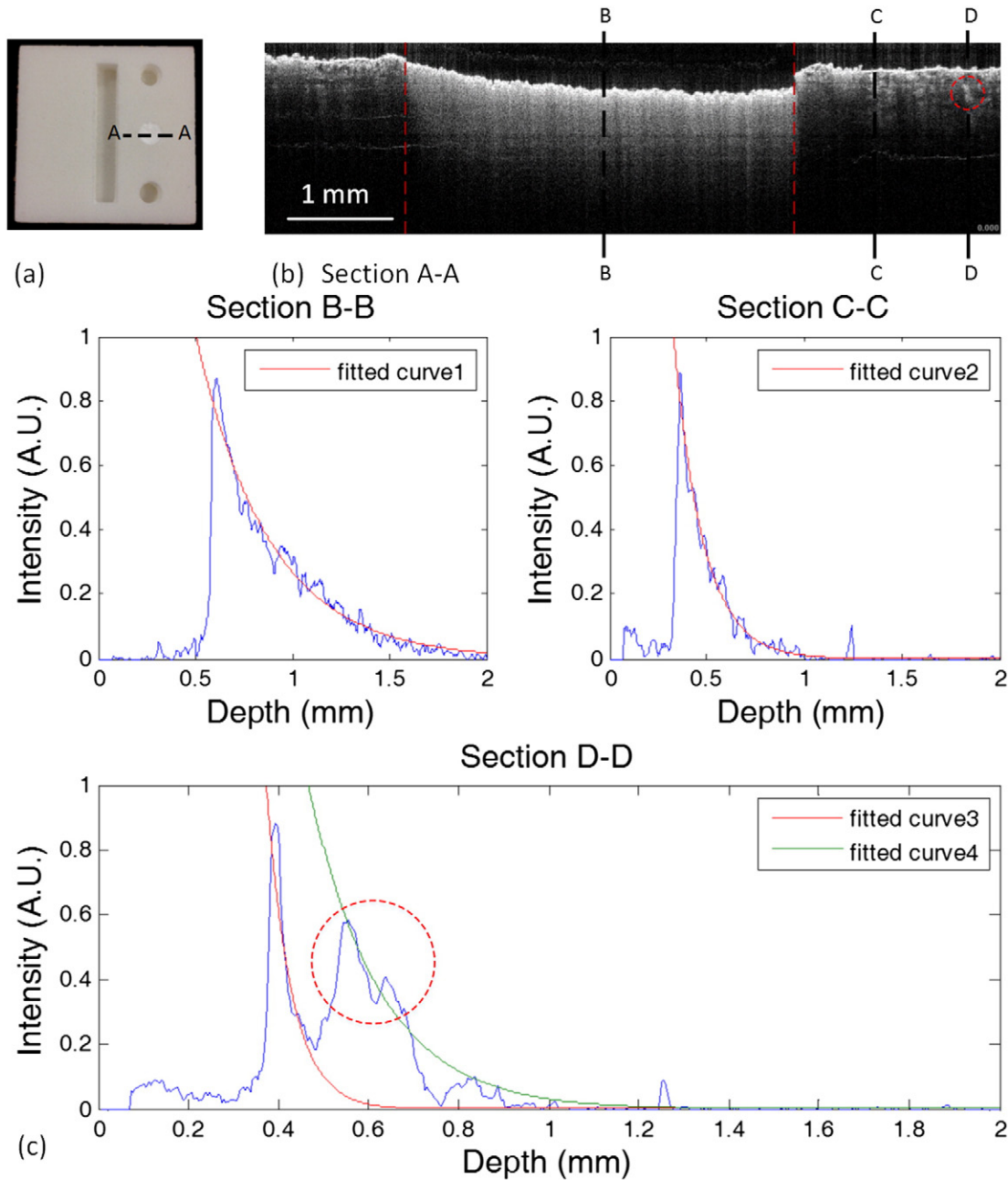


**Fig. 7.** (a) Photograph of specimen from group 3, the section A-A indicates the OCT cross section location; (b) OCT cross-section structure image. The red dashed lines indicate the areas where may contain loose powder; (c) Intensity change through depth at different locations marked by B-B, C-C and D-D in (b). Red dashed circle indicates the high intensity area below the surface.

selective sampling to reduce the scanning area in order to match the 'write' speed of the SLS system. The rapid development of optical sensor and computing technology makes real-time monitoring and control through dynamic feedback a distinct prospect.

Section 3.3 describes OCT's capability for identifying microstructural variations in the solid build, such as poorly melted or unmelted PA2200 powders. One drawback, is that, the measurement accuracy at the highest resolutions will be affected by speckle noise, which is inherent due to the spatial and temporal coherence of the optical waves backscattered from the sample. However, space, time, wavelength or polarization can be dithered to eliminate this noise [27]. This can be done during each sampling interval or, more commonly, in successive scans. The simplest method is to average multiple B-frames, since all these factors will not be identical over the timescale of a frame

acquisition. Alternatively, and perhaps more usefully for this work, the spatially varying nature of the speckle across the image can be used to extract additional information about the sample microstructure [28].

One of the most attractive attributes of OCT is its ability to provide depth-resolved cross-sectional images. This means it has the capability of providing layer-by-layer information for use in defects analysis. In PA2200 for example, the typical penetration depth for quantitative use of OCT images is 200–400  $\mu\text{m}$ . Any void, crack or un-melted powder in this range can be identified and its dimensions can be measured. However, the image depth will be different for different materials since it depends directly on the optical properties (absorption and scattering) of build materials and the wavelength of the OCT light source. This limitation to scanning depth can be overcome by performing real-time

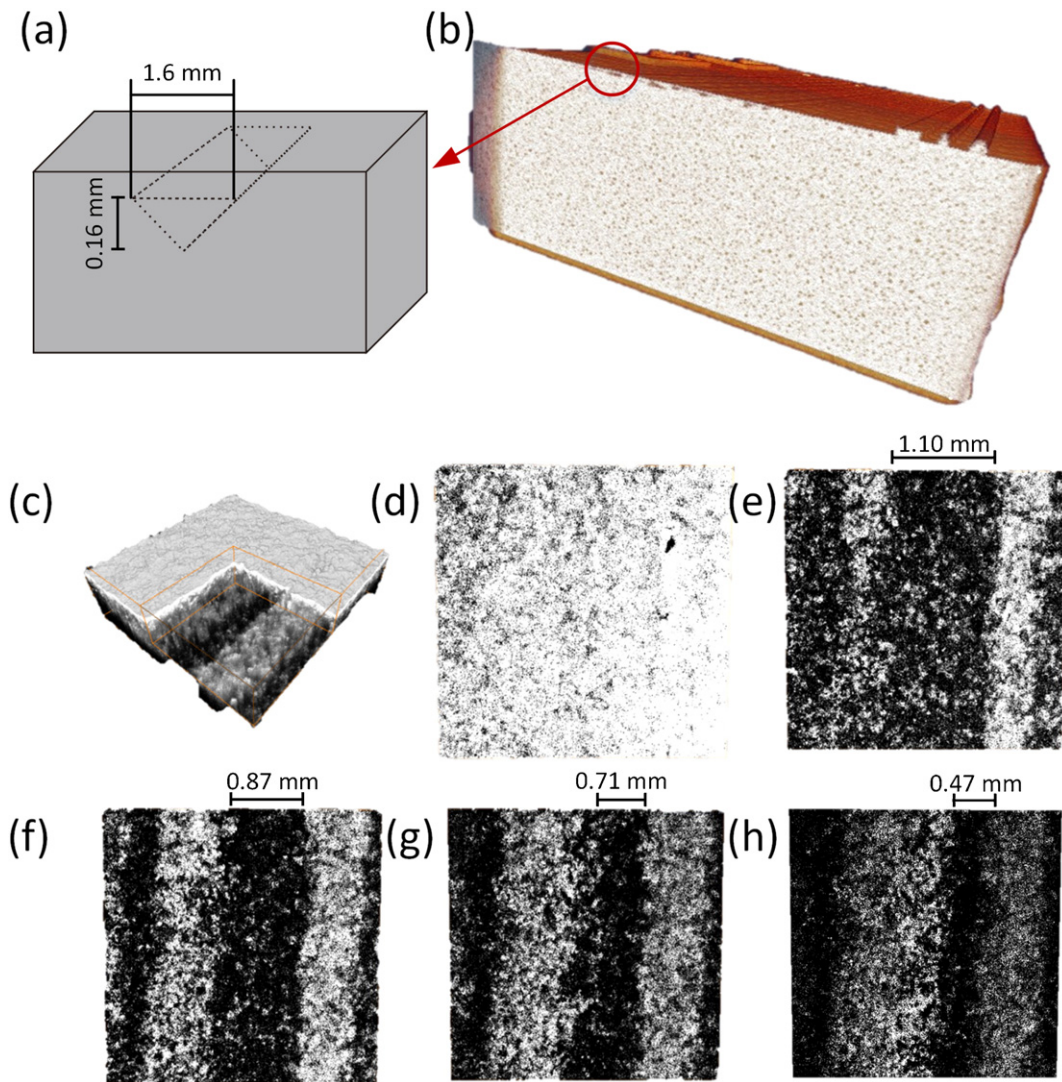


**Fig. 8.** (a) and (b) are design and 3D images of SLS part captured by XCT. The area bound by the red circle identifies the designed void of triangular shape  $\sim 100 \mu\text{m}$  below the surface. (c) is the OCT 3D image for the selected area ( $3 \times 3 \text{ mm}$ ). (d)–(h) show the *en-face* view of this sample at different depths, the darker contrast signifies the void, which becomes narrower with increasing depth.

layer-by-layer scanning, and wavelength tunable OCT systems can be built, to afford flexibility in optimizing the wavelength of the light source for application to specific materials, in order to achieve maximum imaging depth.

## 5. Conclusion

This study has demonstrated the feasibility of using OCT for investigating the surface topography and sub-surface structure of polymeric parts manufactured using SLS. Experiments reported here indicate:

- Typical penetration depths in the range  $200\text{--}400 \mu\text{m}$  are achievable in PA2200 using a commercially available EX1301 OCT system.
- Through OCT it is possible to identify micro-structural variations in the solid build. These may have resulted from feedstock contamination or indeed the reuse of powder. Currently, in post-build NDE methods these observations could not be made.
- Preliminary comparisons between in-situ OCT and XCT of near surface defects indicate that similar results are achieved. However, unlike XCT, OCT conducted in a discrete layer-by-layer approach is a viable technique for performance monitoring.

- Specifically, investigation of 4 sets of samples designed to mimic defects or features commonly found in parts produced by SLS demonstrated: 1)  $<9 \mu\text{m}$  lateral resolution of surface defects such as roughness and local protuberances, 2) roughness and dimensions of open voids built into the part's surface, 3) capability to distinguish between loose and sintered powder  $\sim 200 \mu\text{m}$  below the surface and resolve individual particles down to  $30 \mu\text{m}$  diameter, 4) size and roughness of voids located  $>100 \mu\text{m}$  below the surface.

OCT could therefore present a viable route to real-time, in-situ process monitoring and control during SLS.

## Acknowledgements

The authors acknowledge the grants gratefully received from the UK Engineering & Physical Sciences Research Council (EPSRC), references EP/L017016/1 and EP/L01713X/1. A. T. Clare and K. M. Groom also acknowledge the support provided through the EPSRC Early Careers Forum in Manufacturing Research, through which this collaboration was conceived.

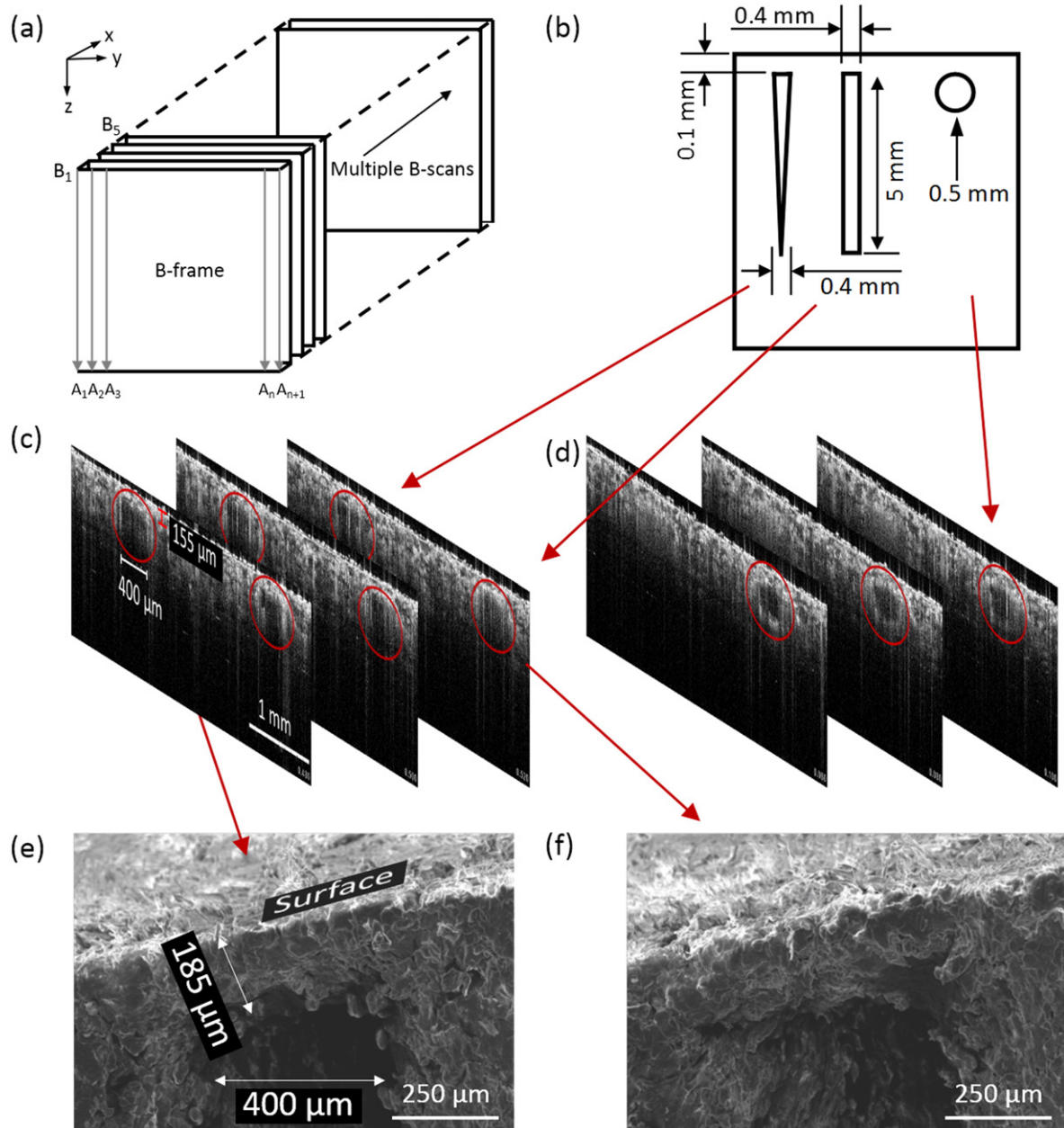


**Fig. 9.** (a) 3D scanning protocol; (b) dimensions of the designed voids; (c), (d) a series of OCT cross-sectional structural images of the sub-surface triangular and square shaped voids and (d) for circles, with a gap of 20  $\mu\text{m}$ ; (e), (f) SEM images for the triangular and square voids.

## References

- [1] I. Gibson, D.W. Rosen, B. Stucker, *Additive Manufacturing Technologies*, Springer, 2010.
- [2] P.F. Jacobs, *Rapid Prototyping & Manufacturing: Fundamentals of Stereolithography*, Society of Manufacturing Engineers, 1992.
- [3] J.-P. Kruth, Material in-process manufacturing by rapid prototyping techniques, *CIRP Ann. Manuf. Technol.* 40 (2) (1991) 603–614.
- [4] N. Tukur, et al., Rapid prototype technique in medical field, *Res. J. Pharm. Technol.* 1 (4) (2008) 341–344.
- [5] J. J. Beaman, and C. R. Deckard, *Selective Laser Sintering With Assisted Powder Handling*, Google Patents (1990).
- [6] C. R. Deckard, *Method and Apparatus for Producing Parts by Selective Sintering*, Google Patents (1989).
- [7] K. Tan, et al., Scaffold development using selective laser sintering of polyetheretherketone–hydroxyapatite biocomposite blends, *Biomaterials* 24 (18) (2003) 3115–3123.
- [8] K. Tan, et al., Selective laser sintering of biocompatible polymers for applications in tissue engineering, *Bio-Med. Mater. Eng.* 15 (1) (2005) 113–124.
- [9] J.M. Williams, et al., Bone tissue engineering using polycaprolactone scaffolds fabricated via selective laser sintering, *Biomaterials* 26 (23) (2005) 4817–4827.
- [10] J.T. Rimell, P.M. Marquis, Selective laser sintering of ultra high molecular weight polyethylene for clinical applications, *J. Biomed. Mater. Res.* 53 (4) (2000) 414–420.
- [11] N. Hopkinson, R. Hague, P. Dickens, *Rapid Manufacturing: An Industrial Revolution for the Digital Age*, John Wiley & Sons, 2006.
- [12] T. Pereira, et al., Effect of process parameters on the properties of selective laser sintered poly (3-hydroxybutyrate) scaffolds for bone tissue engineering: this paper analyzes how laser scan spacing and powder layer thickness affect the morphology and mechanical properties of SLS-made scaffolds by using a volume energy density function, *Virtual Phys. Prototyp.* 7 (4) (2012) 275–285.
- [13] T. Govett, K. Kim, M. Lundin, D. Pinero, *Design Rules For Selective Laser Sintering*, [https://www.me.utexas.edu/~ppmmlab/files/designers\\_guide.sls.pdf](https://www.me.utexas.edu/~ppmmlab/files/designers_guide.sls.pdf)
- [14] G. Ziolkowski, et al., Application of X-ray CT method for discontinuity and porosity detection in 316L stainless steel parts produced with SLM technology, *Arch. Civ. Mech. Eng.* 14 (4) (2014) 608–614.
- [15] F. Léonard et al., "Assessment by X-ray CT of the Effects of Geometry and Build Direction on Defects in Titanium ALM Parts."
- [16] K. Grieve, et al., Ocular tissue imaging using ultrahigh-resolution, full-field optical coherence tomography, *Invest. Ophthalmol. Vis. Sci.* 45 (11) (2004) 4126–4131.
- [17] K. Grieve, et al., In vivo anterior segment imaging in the rat eye with high speed white light full-field optical coherence tomography, *Opt. Express* 13 (16) (2005) 6286–6295.
- [18] C. Li, et al., Detection and characterisation of biopsy tissue using quantitative optical coherence elastography (OCE) in men with suspected prostate cancer, *Cancer Lett.* 357 (1) (2015) 121–128.

- [19] B.J. Vakoc, et al., Cancer imaging by optical coherence tomography: preclinical progress and clinical potential, *Nat. Rev. Cancer* 12 (5) (2012) 363–368.
- [20] T. Yonetsu, et al., Optical coherence tomography—15 years in cardiology, *Circ. J.* 77 (8) (2012) 1933–1940.
- [21] S. Uemura, et al., Thin-cap fibroatheroma and microchannel findings in optical coherence tomography correlate with subsequent progression of coronary atheromatous plaques, *Eur. Heart J.* 33 (1) (2012) 78–85.
- [22] J.P. Dunkers, et al., Optical coherence tomography of glass reinforced polymer composites, *Compos. A: Appl. Sci. Manuf.* 30 (2) (1999) 139–145.
- [23] L. Thrane, et al., Application of optical coherence tomography (OCT) as a 3-dimensional imaging technique for roll-to-roll coated polymer solar cells, *Sol. Energy Mater. Sol. Cells* 97 (2012) 181–185.
- [24] H. Liang, et al., En-face optical coherence tomography — a novel application of non-invasive imaging to art conservation, *Opt. Express* 13 (16) (2005) 6133–6144.
- [25] C. Song, P. Wang, H.A. Makse, A phase diagram for jammed matter, *Nature* 453 (7195) (2008) 629–632.
- [26] C. Lu, et al., Handheld high speed 500 kHz swept source OCT device using a micro scanning mirror, *Invest. Ophthalmol. Vis. Sci.* 54 (6) (2013) 1489.
- [27] J.W. Goodman, Some fundamental properties of speckle, *JOSA* 66 (11) (1976) 1145–1150.
- [28] K.W. Gossage, et al., Texture analysis of optical coherence tomography images: feasibility for tissue classification, *J. Biomed. Opt.* 8 (3) (2003) 570–575.